Multiscale Gas Transport in Shales With Local Kerogen Heterogeneities

I. Yucel Akkutlu, Texas A&M University, and **Ebrahim Fathi,** West Virginia University

Summary

On the basis of micro- and mesoscale investigations, a new mathematical formulation is introduced in detail to investigate multiscale gas-transport phenomena in organic-rich-shale core samples. The formulation includes dual-porosity continua, where shale permeability is associated with inorganic matrix with relatively large irregularly shaped pores and fractures, whereas molecular phenomena (diffusive transport and nonlinear sorption) are associated with the kerogen pores. Kerogen is considered a nanoporous organic material finely dispersed within the inorganic matrix. The formulation is used to model and history match gas-permeation measurements in the laboratory using shale core plugs under confining stress. The results indicate significance of molecular transport and strong transient effects caused by gas/solid interactions within the kerogen. In the second part of the paper, we present a novel multiscale perturbation approach to quantify the overall impact of local porosity fluctuations associated with a spatially nonuniform kerogen distribution on the adsorption and transport in shale gas reservoirs. Adopting weak-noise and mean-field approximation, the approach applies a stochastic upscaling technique to the mathematical formulation developed in the first part for the laboratory. It allows us to investigate local kerogen-heterogeneity effects in spectral (Fourier-Laplace) domain and to obtain an upscaled "macroscopic" model, which consists of the local heterogeneity effects in the real time—space domain. The new upscaled formulation is compared numerically with the previous homogeneous case using finite-difference approximations to initial/boundary value problems simulating the matrix gas release. We show that macrotransport and macrokinetics effects of kerogen heterogeneity are nontrivial and affect cumulative gas recovery. The work is important and timely for development of new-generation shale-gas reservoir-flow simulators, and it can be used in the laboratory for organic-rich gas-shale characterization.

Introduction

Shale-gas-reservoir characterization is important for accurate estimation of the original gas in place, the production rates, the ultimate recovery, and the storage capacity of depleted reservoirs for greenhouse-gas sequestration. Characterization typically includes laboratory measurements of pore volume (PV), permeability and molecular diffusivities, and sorption capacity of selected shale samples. Conventional methods of sampling and measurement of these properties have limited success because of the tight and multiscale nature of the core samples. Shales are relatively low in porosity and have ultralow permeability; in addition, they consist of pores with a wide range of sizes, which often leads to multimodal pore-size distribution. The latter is associated with the diversity of minerals that make up shale, such as clays, carbonates, and organic material (i.e., kerogen) (Wang and Reed 2009; Sondergeld et al. 2010). The complexity in mineral content leads to fundamental-level questions, and often uncertainties, related to the total amounts and spatial distribution of original fluids in the reservoir, their thermodynamic states (i.e., absorbed, adsorbed, or free), and, finally, the mechanisms of their transport under the reservoir conditions. The industry demands development of new sampling/measurement techniques and protocols that would allow fast and accurate predictions of the rock/fluid properties and give consistent and detailed information on the nature of gas storage and transport.

Effective PV of the samples is conventionally measured using the difference between bulk and grain densities. Bulk density is measured using the Archimedes principle by immersing the sample into a mercury bath and measuring the mercury displacement. The displacement equals the bulk volume of the sample. The grain density of the sample, on the other hand, is typically obtained after crushing the sample and using low-pressure gas pycnometry. Gas is introduced into the pycnometer, and pressure change in the pycnometer with and without the crushed sample is measured, which, in turn, is used to determine the grain volume and grain density on the basis of Boyle's law. Typically, helium is used as the measurement gas, although recent experimental analyses indicate that, because of its small molecule size and low adsorption, helium may lead to higher PV estimation with certain organic-rich shale samples that act as a molecular sieve for the measurement gas (Bustin et al. 2008; Kang et al. 2011; Freeman et al. 2011). Mercury porosimetry (or mercury-injection capillary pressure) is another commonly used technique to measure the effective PV. In this case, the sample is placed in a penetrometer. The experiment involves a stepwise increase in penetrometer pressure caused by mercury injection. Because mercury is the nonwetting phase, it would enter only pores that are large enough and accessible at that penetrometer pressure. Thus, by applying sufficiently large pressures, all the interconnected pores in the sample should be reached and hence its PV determined. For shale samples, however, the intrusion of mercury starts at high pressures, typically near 10,000 psi, and, to access the smallest shale pores, the measurement of intrusion volumes often continues up to the maximum capacity of the instrument, typically at 60,000 psi. At that pressure, the instrument cannot detect the contribution of micropores ($d_p < 2$ nm) and some of the mesopores ($d_p < 4$ nm) on the total PV. In addition, there exist a few measurement uncertainties associated with the bulk volume reduction and the applicability of Wasburn's equation.

Several other techniques are available for the measurement of total and effective PVs based on different principles, such as thermogravimetry, nuclear-magnetic-resonance spectrometry, scanning electron microscopy, and low-temperature adsorption porosimetry. However, all of these techniques have their own limitations when the sample under investigation is shale, and suitable instruments are available only in a handful of specialized laboratories.

The PV-estimation techniques have an additional overall limitation, in that the measurements are not performed under the reservoir conditions. In a recent study where we evaluated organic-rich gas-shale reservoirs as an alternative place for carbon dioxide storage (Kang et al. 2011), we argued that pore pressure, temperature, and confining stress conditions could lead to changes in the PV. A new laboratory technique was thus proposed where the gas-pycnometry approach based on Boyle's law has been extended to five-stage pressure/volume-change measurements. The technique uses a 1-in.-diameter core plug in a core holder (not pycnometer) under confining stress, and the five-stage data are used in a nonlinear regression analysis to obtain five parameter values associated with the storage of free and sorbed gas: PV at zero pressure (i.e., true PV), V_{po}; PV compressibility, C_p;

This paper (SPE 146422) was accepted for presentation at the SPE Annual Technical Conference and Exhibition, Denver, 30 October–2 November 2011, and revised for publication. Original manuscript received for review 28 June 2011. Revised paper received for review 27 June 2012. Paper peer approved 6 July 2012.

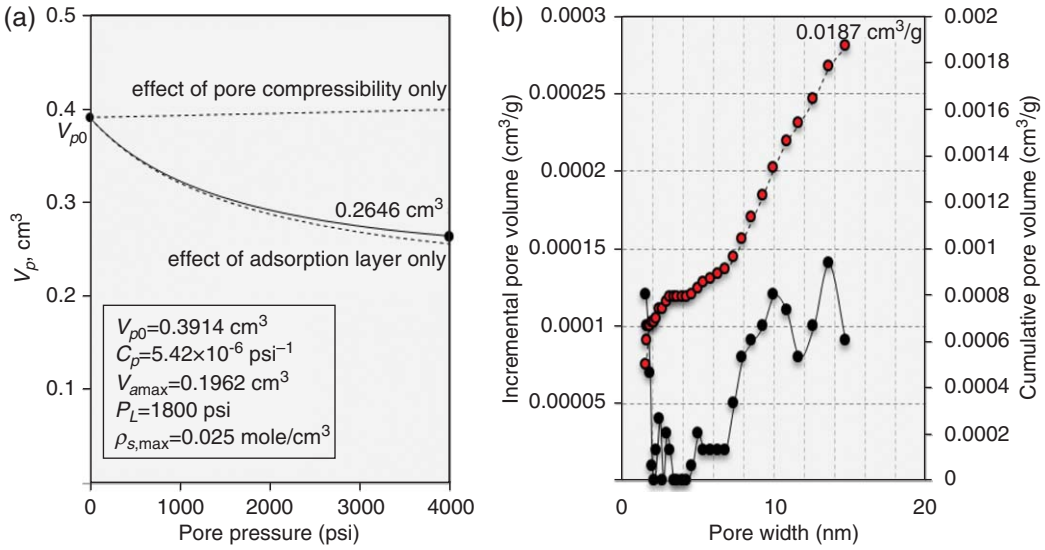

Fig. 1—(a) PV changes with pore pressure for a Barnett shale sample with 3.9% (w/w) total organic content. The five parameters obtained using nonlinear regression analysis are also shown on the figure. The sample is a 2.54 × 4.544-cm disk-shaped core plug that weighs 59.1 g. The confining pressure is 5,000 psi, and the temperature is 298 K. (b) Incremental (solid) and cumulative (dashed) kerogen PV per gram of sample vs. pore width for the same sample. The sample is vacuumed at the reservoir temperature. The kerogen pore-size distribution is obtained using nitrogen adsorption at 77 K and performing density functional theory (DFT) analysis on the obtained adsorption isotherm. The technique detects pores with sizes less than 20 nm only. The distribution is reproduced from Adesida et al. (2011).

Langmuir volume and pressure, $V_{a\max}$ and P_L, respectively; and finally a quantity related to the maximum-density of the adsorbed phase, $\rho_{s,\max}$. **Fig. 1a** shows such estimated values, along with the changes in PV caused by pore pressure, for a Barnett shale sample. The sample has a predicted true PV equal to 0.3914 cm^3. Under initial reservoir pressure of 4,000 psi, its PV drops to 0.2646 cm^3, which is a 32.4% reduction in the pore space. Fig. 1a also shows that the change in PV is caused by pore-compressibility effect and, more importantly, is related to the adsorption layer thickness effect. The adsorption layer affects the PV by taking up some of the pore space available for the free gas. At first glance, this effect might appear to the investigator as trivial; however, adsorption takes place in kerogen in the shale sample, and the sizes of the organic pores are small such that the thickness of the adsorption layer becomes significant. Fig. 1b shows these small organic pores, which are overwhelmingly on a nanometer scale. They take up 0.00187 cm^3 of PV per gram of sample; thus, one would expect that roughly (0.00187 cm^3/g) × 59.1 g ≈ 0.11 cm^3 PV in the core plug is supplied by these nanopores, which is approximately (0.11/0.2646) × 100 ≈ 42% of the total PV under the initial-reservoir-pressure condition.

This reduced PV needs to be used for estimation of the free-gas amount in the core plug; the sorbed amount (both absorbed and adsorbed), on the other hand, can be predicted using an equilibrium adsorption-isotherm value at that pressure. The two parameters of the Langmuir adsorption isotherm are the byproducts of the PV-estimation method summarized previously, and they can also be used for the estimation of the sorbed amount. The total amount of gas in the shale core plug is the sum of the free and the sorbed gas amounts. Further details of the laboratory setup, measurements, and the analysis can be found in Kang et al. (2011). In this paper we would like to emphasize the importance of accurate PV estimation for gas-transport measurements. It is our experience that, because the PV is not treated dynamically and, hence, is not adjusted for the subsurface conditions, the porosity is often overpredicted during routine laboratory measurements. Consequently, transport of a larger volume of fluid is considered during the laboratory analysis, which may lead to larger permeability values.

These are the intricacies associated with the quantification of the shale porosity and the shale gas in place. Before further discussions on shale gas-transport modeling, it is necessary to delve into some additional complexities associated with the spatial distribution of the minerals that make up shale and their impact on the distribution of the gas. **Fig. 2** shows 2D focused-ion-beam/scanning-electron-microscope gas-shale images. In these images, the pores are shown in black, whereas the matrix is represented by gray: dark gray regions are kerogen and light gray regions are inorganic constituents. Clearly, these images show finely dispersed porous kerogen pockets imbedded in inorganic matrix. Using special imaging techniques, our team (Ambrose et al. 2010) has previously shown that these kerogen pockets are interconnected and may include a network of small organic pores with a typical pore-size distribution as shown in Fig. 1b. Note that most of the pores in these images are significantly small, typically less than 100 nm, and are almost exclusively found within the

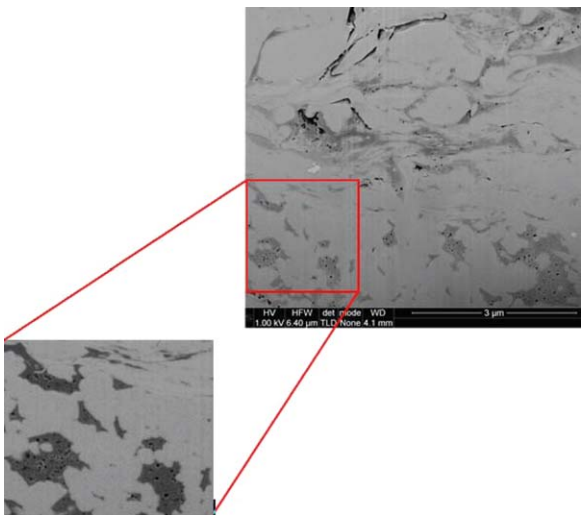

Fig. 2—2D focused-ion-beam/scanning-electron-microscope images of an organic-rich shale sample showing finely dispersed kerogen pockets imbedded in an inorganic matrix. In these images, black depicts pores, dark gray is kerogen, and light gray is inorganic shale matrix with clay and silica dominating. Images are reproduced from Ambrose et al. (2012).

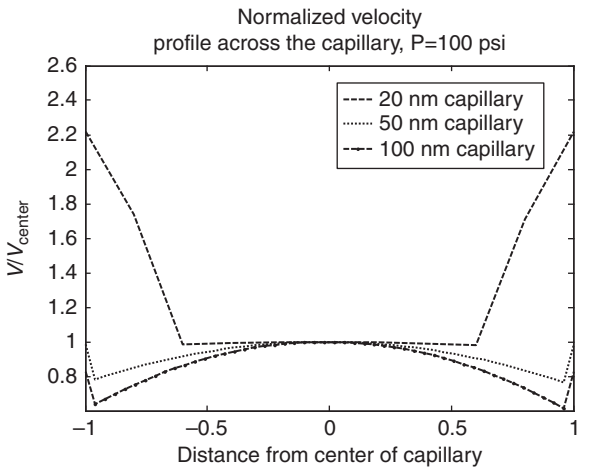

Fig. 3—Steady-state-flow velocity profiles in capillaries with varying diameter at 100-psi average pressure. LBM simulation results include nonparabolic velocity profiles in small pores at low pressures. The velocity is somewhat more uniform (plug-like) at the center of the capillary. For all the capillaries, there exists slippage by the walls. For capillaries with a diameter less than 50 nm, the fluid velocity by the walls is larger than that at the center of the capillary. The wall effect is clearer in the case of a 20-nm pore. $K_n = 0.08058$, $R_e = 3.67 \times 10^{-5}$, $D_S/D_K = 0.01$, and $\mu/\rho = 0.025$ cm^2/s during the simulation of gas dynamics in a 100-nm capillary. $K_n = 0.806$, $R_e = 3.67 \times 10^{-8}$, and $\mu/\rho = 0.025$ cm^2/s during the simulation of gas dynamics in a 10-nm capillary.

kerogen. This also implies that most of the inorganic pores and microfractures have significantly larger dimensions, such as the irregular openings shown in the upper portion of the larger image in Fig. 2. Because of their large sizes, they often may not even appear in these small-scale images. Thus, at a fundamental level, two completely different porous media (i.e., organic and inorganic) are revealed in organic-rich shale. These observations are going to be important later, while we develop the governing equations (coupled nonlinear partial-differential equations) for gas storage and transport in organic-rich shale.

From practical point of view, the organic and inorganic constituents could be considered dual-porosity continua, each having its own gas-storage and mass-transport mechanisms. Inorganic matrix with large pores can store significant amounts of gas under reservoir conditions as compressed gas. Mass transport of this compressed gas is viscous-forces-controlled flow. This transport mechanism is characterized by a parabolic fluid-flow-velocity profile across the pore with no-slip condition (zero velocity) at the pore walls. In petroleum-reservoir simulation, it is a common practice to treat such flow in the reservoir using Darcy's law. In that case, however, it is our experience in the laboratory that the inorganic matrix permeability is quite sensitive to effective-stress conditions in the reservoir, indicating that the inorganic pores are dominantly slit-like in shape or microfracture (rather than cylinder or sphere), because small changes in their size lead to dramatic change in permeability. The microfractures in the inorganics and their impacts on permeability under different confining and pore-pressure conditions have been reported by different groups (e.g., Cui et al. 2009; Javadpour 2009; Sondergeld et. al. 2010a, 2010b; Kang et al. 2011). These have pointed to a need for measuring permeability under effective stress representative of the subsurface conditions. Here, we further investigated the permeability variability under two different conditions: with a constant confining-pore-pressure difference using Sample 1 and with changing effective-stress conditions using Samples 2 and 3.

Gas transport in the kerogen should be treated carefully. Because of the sizes of the organic pores, fluid mechanics of natural gas in kerogen involves nanoscale phenomena, which could lead to potential non-Darcy effects during the gas transport. In general, these are low-Reynolds-number and noncontinuum effects and, more importantly, pore-wall-dominated multiscale effects. **Fig. 3** includes three separate lattice-Boltzmann-method (LBM) simulations of steady gas transport in organic capillaries. It shows the velocity profile across the diameter of each capillary where the computed velocity values (y-coordinate) are normalized by the velocity at the center of the capillary, whereas the distance from the center of the capillary (x-coordinate) is normalized using the diameter of the capillary. The largest capillary is 100 nm in diameter (shown in dash-dot). The normalized velocity profile across this capillary shows a parabolic trend, which indicates the presence of viscous coupling inside the capillary. Accordingly, one would hastily observe that the continuum flow is valid, and thus Darcy's law can still be used as the constitutive relationship to describe the flow in large organic pores. In Fathi and Akkutlu (2011), we argued this is the case for organic pores with sizes larger than 100 nm. If one looks carefully at the velocity profile across the large capillary shown in Fig. 3, however, one finds that, unlike the continuum flow, the fluid velocity at the walls is nonzero! Furthermore, locally high velocities exist inside the capillary near the walls. The enhanced transport of gas by the walls is molecular streaming caused by slipping and bouncing-back effects of molecules interacting with the walls. These gas wall interactions occur at large (small) Knudsen numbers (capillaries). Consequently, gas transport in organic capillaries smaller than 100 nm goes through a transition in flow regime such that the predicted gas transport is somewhat enhanced. The other velocity profiles in Fig. 3 correspond to gas transport in smaller organic capillaries. Note that because of increased pore-wall effects, the molecular streaming is now dominant, and the parabolic profile is replaced with a uniform (diffusive) velocity profile at the center of the pore. King (2007), investigating gas flow in circular nanotubes, made similar observations. On the basis of these results, we expect that the transport in smaller capillaries (< 10 nm) and at low pressures is caused mainly by molecular streaming and, to a lesser extent, pore diffusion.

In Kang et al. (2011) and Fathi and Akkutlu (2011), we argued the possibility of another transport mechanism that appears in organic capillaries at higher pore pressures. This mechanism, also known as solid or surface transport (hopping of the molecules by the walls), is also diffusive but driven by the local gradients in the adsorbed-phase density. Hopping could dominate the molecular transport in kerogen, particularly when the pore network is yet not well-developed and, hence, the fluid molecules could only permeate through the organic solid with micropores.

The results of this section point to the existence of a critical pore size for the onset of laminar gas flow. Below this critical size, the predicted velocity profile shows the slippage (at low pressure) and hopping (at high pressure) mechanisms leading to molecular-streaming effects by the pore walls, enhancing the gas transport in the organic pores. The traditional permeability-measurement methods that treat shale as a single-porosity and single-permeability medium should then predict high apparent permeability values resulting from the presence of molecular transport in organic pores. Note, however, that, although a few large organic pores could allow development of continuum flow, the kerogen pockets overall should not have a physically meaningful permeability. For further discussions on the LBM, see Succi (2001) and Sukop and Thorne (2006), and for the simulations (LBM-Ls) on the pore-wall-dominated molecular-streaming effect on gas dynamics, see Fathi and Akkutlu (2011, 2012b).

In summary, the gas transport in organic-rich shales involves a matrix with dual-porosity continua associated with organic and inorganic pores, and a fracture continuum. **Fig. 4** shows the conceptual model proposed for the matrix/fracture system. According to this interpretation, the gas transport is in series. Hence, the kerogen pore network communicates hydraulically with the inorganic matrix such that transport takes place in the following sequence during the gas release: organic → inorganic → fracture. Dietrich et al. (2005) argue that the application of multicontinua requires that each porous medium be distributed continuously in space and hold the porous-medium conditions specified by Bear and

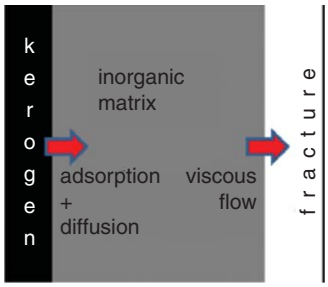

Fig. 4—Multicontinuum approach for shale gas transport in series.

Bachmat (1991). Governing equations describing the gas mass balance in dual continua are the same as in a single-continuum model; however, they need special considerations for volume consistency and the mass-exchange terms.

For free gas mass balance in the kerogen,

$$\frac{\partial(\varepsilon_{kp}\phi\, C_k)}{\partial t}+\frac{\partial[\varepsilon_{ks}(1-\phi-\phi_f)\, C_\mu]}{\partial t} =\frac{\partial}{\partial x}\left(\varepsilon_{kp}\,\phi D_k\frac{\partial C_k}{\partial x}\right)+\frac{\partial}{\partial x}\left(\varepsilon_{ks}(1-\phi-\phi_f)\, D_s\frac{\partial C_\mu}{\partial x}\right). \quad \ldots\ldots\ldots\ldots\ldots\ldots (1)$$

Here, x and t are the space and time coordinates, respectively. $C_k(x,t)$ and $C_\mu(x,t)$ represent the amounts of free gas and adsorbed phase in kerogen in terms of moles per kerogen PV and moles per kerogen solid volume, respectively. In Eq. 1, ϕ and ϕ_f are the total interconnected matrix porosity and fracture porosity in shale, respectively. As explained earlier, these dynamic quantities may vary significantly in time and space because of the void-volume compressibility and adsorption-layer effects with the changing pore pressure. ε_{ks} is the total organic content (TOC) in terms of organic grain volume per total grain volume, and ε_{kp} is kerogen PV per total matrix PV. Hence, $\varepsilon_{kp}\phi$ is equal to kerogen porosity ϕ_k, and it can be written in terms of the bulk volume, total PV, and kerogen PV as $\phi_k=(V_{kp}/V_p)(V_p/V_b)$. Similarly, $\varepsilon_{ks}(1-\phi-\phi_f)$ is the fractional kerogen solid volume (i.e., $1-\phi_k$), which can be written in terms of volumes as $1-\phi_k=(V_{ks}/V_{ms})(V_{ms}/V_b)$. Here V_{kp} and V_{ks} are the kerogen pore and grain volumes and V_{ms}, V_p, and V_b are grain, pore, and bulk volumes for the matrix, respectively. In Eq. 1, D_k is the tortuosity-corrected coefficient of diffusive molecular transport for the free gas in kerogen. Finally, D_s is the coefficient of diffusive molecular transport for the adsorbed gas in kerogen (i.e., hopping). The diffusion coefficients are considered in terms of a total mass flux, which is, for simplicity in the analysis of the experimental work, taken as Fickian in nature. Note that the subscripts k, m, and f refer to quantities related to the kerogen, inorganic matrix, and fracture, respectively.

For adsorbed-phase mass balance in the kerogen,

$$\frac{\partial C_\mu}{\partial t}=k_{\text{desorp}}[K(C_{\mu s}-C_\mu)C_k-C_\mu]. \quad \ldots\ldots\ldots\ldots (2)$$

Here, $C_{\mu s}$ is maximum monolayer gas adsorption on the internal kerogen solid surfaces, $K=k_{\text{ads}}/k_{\text{desorp}}$ is often referred to as the equilibrium partition (or distribution) coefficient, and k_{ads} and k_{desorp} are adsorption- and desorption-rate coefficients, respectively. Several authors have previously studied the nonlinear sorption kinetics behavior of gas; see, for example, Srinivasan et al. (1995) and Schlebaum et al. (1999). Eqs. 1 and 2 thus allow us to keep track of the adsorbed amount in kerogen under nonequilibrium sorption conditions. In the limit $\partial C_\mu/\partial t$=0, Eq. 2 is reduced to the well-known Langmuir isotherm representing adsorption under equilibrium conditions.

For free-gas mass balance in the inorganic matrix,

$$\frac{\partial[(1-\varepsilon_{kp})\,\phi\, C]}{\partial t}=\frac{\partial}{\partial x}\left[(1-\varepsilon_{kp})\,\phi D\frac{\partial C}{\partial x}\right] +\frac{\partial}{\partial x}\left[(1-\varepsilon_{kp})\,\phi\, C\frac{k_m}{\mu}\frac{\partial p}{\partial x}\right]-W_{km}, \quad \ldots\ldots\ldots\ldots (3)$$

where $(1-\varepsilon_{kp})\phi$ is the inorganic porosity (i.e., ϕ_I). D is the tortuosity-corrected coefficient of diffusive molecular transport in the inorganic matrix, k_m is the absolute permeability of the matrix, and μ is the dynamic gas viscosity. Mass exchange between two continua is captured by a coupling term, W_{km}, which is a function of shape factor ℓ, diffusive transport Ψ, and the concentration difference between the two continua at the interface, as given in Eq. 5.

For free-gas mass balance in fracture network:

$$\frac{\partial(\phi_f C_f)}{\partial t}=\frac{\partial}{\partial X}\left(\phi_f K_L\frac{\partial C_f}{\partial X}\right)+\frac{\partial}{\partial X}\left(C_f\frac{k_f}{\mu}\frac{\partial p_f}{\partial X}\right)-W_{mf}, \quad \ldots\ldots\ldots\ldots\ldots (4)$$

which is convective-dispersive. The mass transfer functions introduced in Eqs. 3 and 4 are defined as

$$W_{km}=\ell_m\Psi_k(C-C_k) \quad \ldots\ldots\ldots\ldots\ldots (5)$$

$$W_{mf}=\ell_f\Psi_m(C_f-\overline{C}). \quad \ldots\ldots\ldots\ldots\ldots (6)$$

In mass-exchange terms, $\ell\,\Psi$ has a dimension of 1/time that corresponds to the resistance time for mass exchange between different media.

Transport Model for Shale-Gas Core Plugs

These equations can be reduced to a simpler form that can be used for a gas mass storage and transport study in the laboratory using gas-permeation experiments and pressure-pulse-decay analysis. For this purpose, we considered that the pressure pulses applied are small such that the temporal changes in PVs are negligible across the shale sample. The thermodynamic behavior of free gas can be represented by the compressibility equation of state $p=zCRT$. Furthermore, under confining-stress conditions, it is assumed that the artificially induced and desiccation fractures would be closed and ineffective. Hence, any existing microfracture effects are considered part of an effective inorganic permeability. Consequently, the pulse decay could be analyzed in the absence of Eqs. 4 and 6. Finally, molecular diffusion in the inorganic pores and microfractures is small compared with viscous flow and can be ignored. Thus, the governing equations become

$$\varepsilon_{kp}\phi\frac{\partial C_k}{\partial t}+\varepsilon_{ks}(1-\phi)\frac{\partial C_\mu}{\partial t}=\frac{\partial}{\partial x}\left(\varepsilon_{kp}\phi D_k\frac{\partial C_k}{\partial x}\right) +\frac{\partial}{\partial x}\left[\varepsilon_{ks}(1-\phi)D_s\frac{\partial C_\mu}{\partial x}\right] \quad \ldots\ldots\ldots\ldots\ldots (7)$$

$$\frac{\partial C_\mu}{\partial t}=k_{\text{desorp}}[K(C_{\mu s}-C_\mu)C_k-C_\mu] \quad \ldots\ldots\ldots\ldots (8)$$

$$(1-\varepsilon_{kp})\phi\frac{\partial C}{\partial t}=\frac{\partial}{\partial x}\left[(1-\varepsilon_{kp})\phi zRTC\frac{k}{\mu}\frac{\partial C}{\partial x}\right] -(1-\varepsilon_{kp})\phi\ell_m\left(D-\frac{C_\mu}{C-C_k}D_s\right)(C-C_k) \quad \ldots\ldots\ldots (9)$$

Eqs. 7 through 9 can be transformed into a compact form using the definitions of ϕ_k and ϕ_I as follows:

$$\phi_k\frac{\partial C_k}{\partial t}+(1-\phi_k)\frac{\partial C_\mu}{\partial t}=\frac{\partial}{\partial x}\left(\phi_k D_k\frac{\partial C_k}{\partial x}\right) +\frac{\partial}{\partial x}\left[(1-\phi_k)D_s\frac{\partial C_\mu}{\partial x}\right] \quad \ldots\ldots\ldots\ldots\ldots (10)$$

$$\frac{\partial C_\mu}{\partial t}=k_{\text{desorp}}[K(C_{\mu s}-C_\mu)C_k-C_\mu] \quad \ldots\ldots\ldots\ldots (11)$$

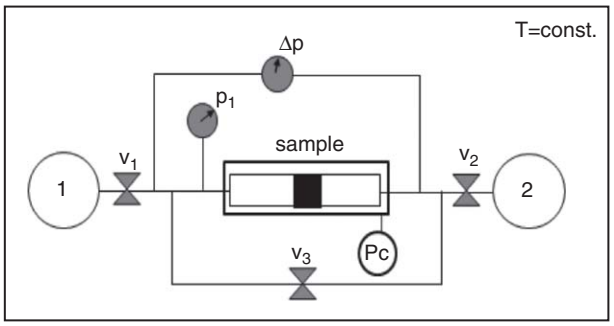

Fig. 5—Schematic of pressure-pulse-decay apparatus.

$$\phi_I \frac{\partial C}{\partial t} = \frac{\partial}{\partial x}\left(\phi_I zRTC\frac{k}{\mu}\frac{\partial C}{\partial x}\right) - \phi_I \ell_m\left(D - \frac{C_\mu}{C - C_k}D_s\right)(C - C_k). \quad \cdots\cdots\cdots\cdots\cdots\cdots (12)$$

Eqs. 10 through 12 define gas transport in series and are consistent with the micro- and mesoscale petrophysical observations made earlier. Together with appropriate initial/boundary conditions, these equations make up the theoretical model that will be used to investigate gas transport in the laboratory and, later, macrotransport and macrokinetics effects of local kerogen heterogeneities.

Pressure-Pulse-Decay Experiments

Steady-state methods of permeability measurement are not practical because of very low flow rates and the extremely long time needed to reach the steady condition. Therefore, transient methods based on pressure-pulse-decay measurements have been used extensively to estimate permeability of the shale samples (Brace et al. 1968; Ning 1992; Finsterle and Persoff 1997). The transient methods are faster and can be used to measure permeabilities as low as 10^{-9} mD (Ning 1992).

Fig. 5 shows a schematic of the apparatus used to perform the pressure-pulse-decay experiment of this study. There are two upstream and downstream reference cells (1 and 2); a 1.0-in.-diameter core-plug sample is placed in the core holder, and confining pressure is applied to resemble the reservoir condition. The sample holder and the reference cells are then filled with the measurement gas to the pressure of interest within a range of 1,000 to 4,000 psi, and enough time is allowed to make sure the measurement system reaches thermodynamic equilibrium conditions. Next, a small pulse is applied by rapidly decreasing the downstream pressure approximately 10% of the equilibrium pressure. As the consequence of the pulse applied, gas starts permeating from the upstream end of the sample to the downstream. The upstream pressure declines during the gas permeation. The decline curve is generated by measuring the upstream pressure in small time intervals. **Fig. 6** shows example pressure-decline curves for two shale samples. A typical pressure decay has two distinct behaviors with completely different characteristic times. At early times, the decay is characterized by a rapid decline in pressure (i.e., fast transport) and later by a gradual decline (i.e., slow transport).

Having generated the pressure-decline curve experimentally, next we used a simulation-based history-matching algorithm called randomized maximum likelihood (RML) to estimate the transport properties of the dual-porosity, single-permeability model given by Eqs. 10 through 12. **Fig. 7** shows the workflow diagram for the history-matching process. For the simulations, initial and boundary conditions consistent with the experimental model are used. During the optimization, we use Langmuir parameter values and total PV corrected for PV compressibility and adsorption-layer effects, as described earlier. TOC measurements are performed independently.

History-Matching Algorithm Using RML

RML algorithm is a simulation-based minimization method that has been used to generate realizations honoring observation data (i.e., upstream pressure decline curve) and carrying out prior knowledge about the model variables (e.g., kerogen PV, inorganic matrix permeability, molecular diffusion coefficients, etc.) and their spatial correlations. In this method, the prior model variables and observation data are updated by adding unconditional realizations of them with their covariance matrices. Oliver et al. (1996) investigated the application of the RML method in conditioning permeability data to pressure data. They showed that RML is effective in sampling from multimodal univariate distributions because it minimizes both data mismatch and distance from unconditional realizations. In cases where it is necessary to limit the number of realizations, the RML method provides better results than other methods, such as the Markov Chain Monte Carlo (MCMC) method (Liu and Oliver 2003). For the minimization purpose, a Levenberg-Marquardt algorithm is used to determine the best model variables that minimize the objective function for each realization. The basic Levenberg-Marquardt algorithm for minimizing an arbitrary objective function $O(m)$ simply replaces $N_m \times N_m$ Newton Hessian matrix H_n at the nth iteration by $H_n + \lambda_n I$, where I is the $N_m \times N_m$ identity matrix and $\lambda_n \geq 0$ is chosen to obtain an improved downhill search direction. In our case, the objective function is defined as follows:

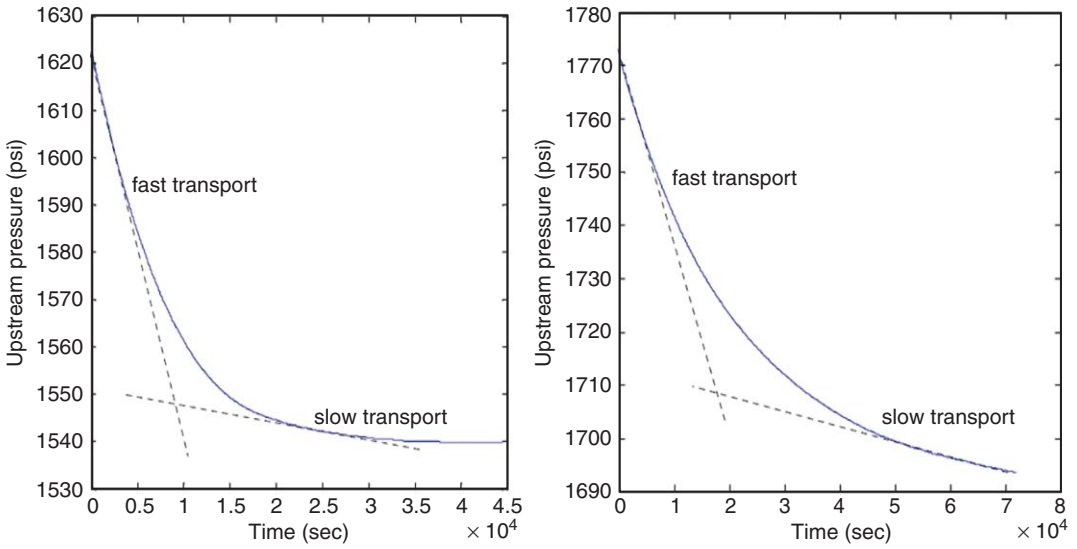

Fig. 6—Pressure-transient curve for shale Sample 2 showing fast- and slow-transport mechanisms.

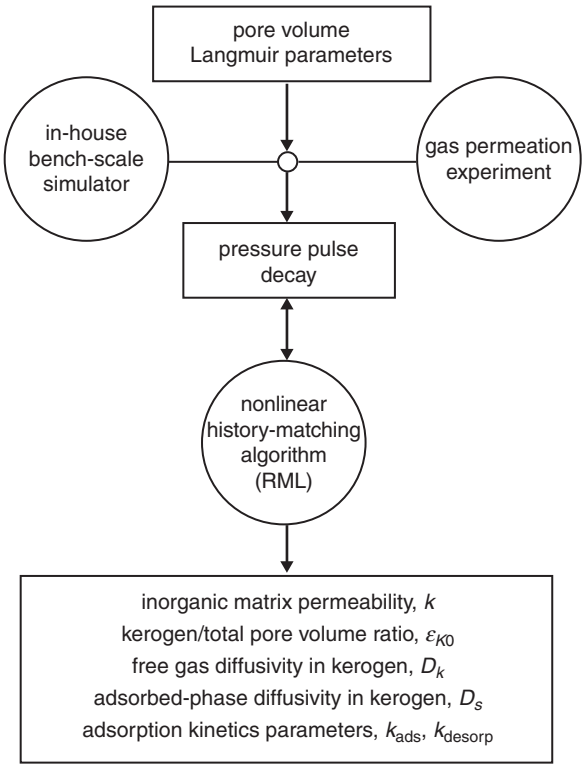

Fig. 7—Workflow diagram for shale matrix rock and transport properties.

$$O(m) = \frac{1}{2}(m - m_{ui})^T C_M^{-1}(m - m_{ui}) + \frac{1}{2}[d_{ui} - g(m)]^T C_D^{-1}[d_{ui} - g(m)], \quad \ldots\ldots\ldots (13)$$

where m is a vector of model variables that minimizes the objective function O, whereas C_M and C_D are the model variables, and data covariance matrices m_{ui} and d_{ui} are the unconditional realizations of model variables and data. g is the theoretical model describing the relation between model variables and the observation data. Further details of the minimization can be found in Oliver et al. (2008).

The pressure-decline curve obtained using pressure-pulse-decay experiment is history matched by a number of realizations (typically 100 realizations); consequently, histograms of rock and transport parameters are obtained. **Fig. 8** shows an example history-matching process for shale Sample 1. The measured upstream pressure decline is shown in blue, and 122 realizations matching the data are shown in red. It is clear that the history-matching algorithm could match the experimental data and shows a reasonable amount of uncertainty associated with predictions. In **Fig. 9,** histograms of predicted parameters from 122 realizations are illustrated.

In **Table 1,** the analysis of pressure-pulse-decay data is given for shale samples with varying TOC. Separate pulses are completed for each sample at equilibrium pore-pressure values varying between 150 and 3,000 psi so that the impact of effective stress on the estimated parameters can be investigated. Porosity in this table represents the void volume available for free gas only; hence, porosity has been corrected for the pore-compressibility and methane-adsorption effects as explained for Fig. 1; TOC is measured independently. Note that the first sample is kept under constant confining pore-pressure difference, whereas the other two samples are measured under constant confining pressure but with varying pore pressure. Thus, the predicted transport coefficients k, D_k, and D_s of the first sample decrease and the other two samples increase with the pore pressure. This can be caused by the sensitivity of the microfractures or pore throats to effective-stress conditions, although the contribution of their PVs in effective total porosity is small.

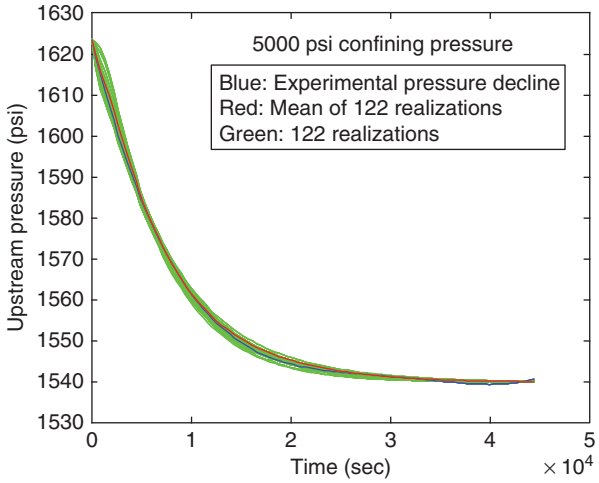

Fig. 8—History-matching results of upstream pressure-decline curve of Sample 2 using dual-porosity single-permeability model in series.

The results for Sample 1 indicate that gas desorption takes place fast because of large k_{desorp} value, and the predicted transport in kerogen is molecular (free-gas) diffusion. Because the pore pressures are high, gas/wall interactions represented by slipping and bouncing back of gas molecules are not present. In addition, because the adsorbed-phase gradient (dC_μ/dx) is typically small across the plug, it is concluded that the surface diffusion (hopping) does not play an important role in gas transport in Sample 1. This is consistent with the D_s/D_k ratio value used in Fig. 3. The results associated with the other two samples are quite different, however. Table 1 shows that the surface diffusion coefficient is significantly higher for Samples 2 and 3 compared with the molecular diffusion. Typically, the obtained values give significantly higher D_s/D_k compared with the value observed with Sample 1 and the value used in Fig. 3. This may indicate that the kerogen pore network is not fully developed and, hence, not interconnected; consequently gas transport in the kerogen is nanoporous solid-controlled. In general, 35 to 67% of total PV of the samples is associated with the kerogen, indicating that kerogen can contribute to gas storage although TOC (measured in terms of weight percentage) is quite low for all the samples.

Fig. 10 shows three pressure pulse decays for Sample 2 under constant confining pressure. Note that the measured upstream pressure is normalized with the final equilibrium pressure; hence, all the curves converge to unity at large times. It shows that the time to reach final equilibrium becomes much shorter as the pore pressure increases. This indicates faster gas transport at higher pore pressures. These observations are consistent with the previous observations by other groups (Cui et al. 2009; Javadpour 2009; Sondergeld et al. 2010a, 2010b; Kang et al. 2011).

Upscaled Governing Equations for Gas Transport in Shales with Kerogen Heterogeneity

The analysis of the previous experimental section using shale core plugs indicates that kerogen is an important component of shale because it participates in both gas-storage and -transport processes. Independent studies by Schettler and Parmely (1991) and Freeman et al. (2011) also showed the importance of the kerogen component of shale in total storage. However, more investigations conducted by different research groups are still needed to elaborate on these fundamental observations and to make remarks on how early gas stored in kerogen could be recovered during the production. Here, we approach the problem independently using a theoretical (stochastic) approach that allows us to investigate the role kerogen plays in the transport of the gas in organic shale. If kerogen contributes to the total porosity of shale and if the transport mechanisms in the kerogen are important, as observed above using the experimental gas-permeation data, then spatially

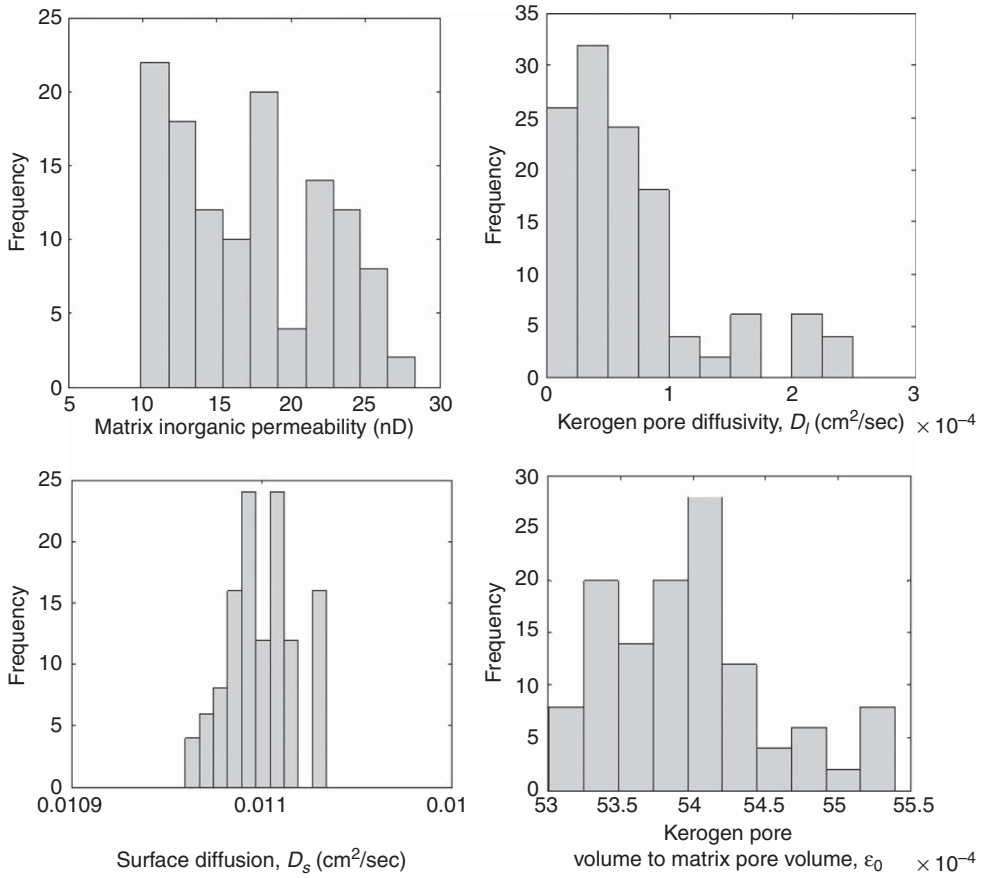

Fig. 9—Histograms of predicted rock and transport parameters of Sample 2 at 1,623-psi equilibrium pressure (Table 1). Estimated gas (methane) transport parameters for shale samples with varying TOC using pulse-decay and gas-permeation experiments.

random fluctuations in the kerogen amount would potentially influence the nature of both storage and transport across the shale. Such a hypothesis could be tested using the small-fluctuations theory (Fathi and Akkutlu 2009, 2012a) or other upscaling approaches used by different groups and discussed in detail by Cushman et al. (2002).

A naturally occurring porous-medium heterogeneity is thus introduced as a time-independent, spatially variable random

TABLE 1—PRESSURE-PULSE-DECAY DATA FOR THREE DIFFERENT SHALE SAMPLES WITH VARYING TOC

Effective Stress Conditions		Pulse		Estimated Matrix Parameters					
					Inorganic	Kerogen			
Confining Pressure (psi)	Equilibrium Pore Pressure (psi)	ΔP (psi)	Time to Reach Equilibrium (sec)	ϕ%	k nD	ε_k (vol/vol)%	D_k cm^2/s	D_s cm^2/s	k_{desorp} 1/s
Sample 1 (TOC 0.6%)									
	0			4.2					
1,150	158	82	75,600	4.1	76.0	34.0	1.4×10^{-4}	5.1×10^{-4}	9.0×10^{-4}
2,000	1,019	79	20,700	4.0	22.1	34.2	4.7×10^{-4}	8.3×10^{-4}	9.0×10^{-4}
3,000	2,012	81	23,100	4.1	13.5	39.0	4.4×10^{-4}	1.0×10^{-3}	9.0×10^{-4}
4,000	2,966	88	22,620	4.3	9.67	36.3	3.9×10^{-4}	1.0×10^{-3}	9.0×10^{-4}
Sample 2 (TOC 3.9%)									
	0			1.7					
5,000	1,623	83	44,485	1.3	17.1	53.9	7.0×10^{-5}	1.1×10^{-2}	1.4×10^{-7}
5,000	2,588	84	18,063	1.2	20.4	64.2	4.0×10^{-5}	4.2×10^{-2}	1.5×10^{-7}
5,000	2,974	70	12,060	1.2	28.7	67.6	4.9×10^{-5}	8.8×10^{-2}	1.5×10^{-7}
Sample 3 (TOC 4%)									
	0			2.9					
5,000	1,772	78	72,060	2.4	2.6	43.6	3.5×10^{-5}	1.1×10^{-3}	1.0×10^{-7}
5,000	2,500	74	54,480	2.3	3.5	47.1	5.3×10^{-5}	2.5×10^{-3}	1.3×10^{-7}
5,000	3,066	73	32,520	2.3	5.2	48.2	8.2×10^{-5}	4.6×10^{-3}	1.5×10^{-7}

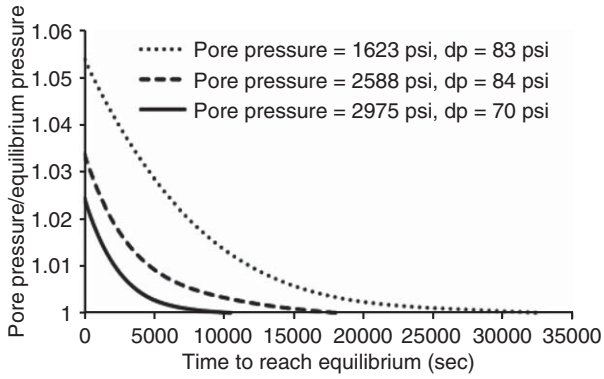

Fig. 10—Time to reach equilibrium at different pore pressure and similar pulse for Sample 2.

kerogen porosity field $\phi_k = \overline{\phi}_k + \tilde{\phi}_k$ in terms of its mean $\overline{\phi}_k$ and small fluctuation $\tilde{\phi}_k$, whereas inorganic porosity, ϕ_I, and permeability, k, are kept constant. Further, it is considered that the kerogen porosity obeys stationarity of moments of order 1 and 2 (hence, mean and the variance of kerogen porosity are kept constant) with a well-defined spatial covariance function. All the dependent variables, transport, and rate coefficients are affected by the medium heterogeneity presented by the kerogen-porosity random field; therefore, they are also considered to be random variables. Consider that an overbar and a tilde over a quantity denote its average value and its fluctuations about the mean, respectively. We then have

$$\alpha_1 = \overline{\alpha}_1 + \tilde{\alpha}_1,$$
$$\alpha_2 = \overline{\alpha}_2 + \tilde{\alpha}_2,$$
$$\alpha' = \overline{\alpha}' + \tilde{\alpha}',$$
$$C_k = \overline{C}_k + \tilde{C}_k,$$
$$C = \overline{C} + \tilde{C},$$
$$C_\mu = \overline{C}_\mu + \tilde{C}_\mu,$$
$$D_k = \overline{D}_k + \tilde{D}_k,$$
$$D_s = \overline{D}_s + \tilde{D}_s,$$
$$\Phi_k = \overline{\Phi}_k + \tilde{\Phi}_k,$$

and

$$K = \overline{K} + \tilde{K},$$

where we introduce $\alpha_1 = \partial(\phi_k D_k)/(\phi_k \partial x)$ as an effective drift velocity, reflecting changes in free-gas concentration caused by a nonconstant diffusivity with a gradient and $\alpha_2 = \partial[(1-\phi_k)D_s]/(\phi_k \partial x)$ as an effective drift velocity of adsorbed phase resulting from a nonconstant surface diffusion coefficient with a gradient. In addition, we define $\alpha' = \partial(\phi_k C_k)/(\phi_k \partial x)$, $\beta = kRT/\mu$ (the gas mobility), and $\Phi_k = (1-\phi_k)/\phi_k$ as the solid-to-bulk kerogen volume ratio.

Two sets of equations can be derived by substituting the perturbed quantities into Eqs. 10, 11, and 12. These are the mean equations and the perturbation equation. The mean equations are the upscaled governing equations, including a series of auto- and cross-correlations between perturbed quantities. Expressions for these correlations are found using general solutions for the free- and adsorbed-gas concentrations in the Laplace-Fourier domain. Thus, new upscaled governing equations are obtained that include the effects of local variations in kerogen porosity. Details on the methodology, the correlation functions, and upscaling can be found in Forster (1975), Gelhar (1993), L'Heureux (2004), and, more recently, in Fathi and Akkutlu (2009, 2012a). Following their approach, the new upscaled governing equations for gas transport in dual-continua shale matrix are presented as follows:

$$\overline{\phi}_k \frac{\partial \overline{C}_k}{\partial t} + (1-\overline{\phi}_k)\frac{\partial \overline{C}_\mu}{\partial t} = \frac{\partial}{\partial x}\left(\overline{\phi}_k D_{k_{\text{eff}}} \frac{\partial \overline{C}_k}{\partial x}\right) + \frac{\partial}{\partial x}\left[(1-\overline{\phi}_k) D_{s_{\text{eff}}} \frac{\partial \overline{C}_\mu}{\partial x}\right] + \Gamma_{tr} \quad \ldots\ldots\ldots\ldots\ldots\ldots (14)$$

$$\frac{\partial \overline{C}_\mu}{\partial t} = k_{\text{desorp}}[\overline{K}(C_{\mu s} - \overline{C}_\mu)\overline{C}_k - (\overline{C}_\mu + \Gamma_{kn})] \quad \ldots\ldots\ldots (15)$$

$$\phi_I \frac{\partial \overline{C}}{\partial t} = \frac{\partial}{\partial x}\left(\phi_I z R T \overline{C} \frac{k}{\mu}\frac{\partial \overline{C}}{\partial x}\right) - \phi_I \ell_m \left(\overline{D} - \frac{\overline{C}_\mu}{\overline{C} - \overline{C}_k}\overline{D}_s\right)(\overline{C} - \overline{C}_k) + \Gamma_{ex}. \quad \ldots (16)$$

In Eq. 14, the diffusion coefficients are effective quantities, although their values are not significantly different from those local values of D_k and D_s. In addition, we have Γ_{tr} and Γ_{kn}, which have previously been identified in Fathi and Akkutlu (2009) as the macrotransport and macrokinetics effects of local kerogen-porosity heterogeneities, respectively. They are defined as

$$\Gamma_{tr} = (1 - \upsilon_1 \upsilon_2 \overline{C}_k)\overline{\phi}_k \sigma^2_{\phi k} \overline{C}_{\mu,0} \quad \ldots\ldots\ldots\ldots\ldots (17)$$

$$\Gamma_{kn} = \upsilon_1 (1 + \upsilon_1 \upsilon_2 \overline{C}_k)\frac{N_{\text{Th}}}{k_{\text{desorp}}} \sigma^2_{\phi k} \overline{C}_{\mu,0}. \quad \ldots\ldots\ldots\ldots (18)$$

The contribution of the macrokinetics and macrotransport effects have previously been analyzed in detail by Fathi and Akkutlu (2009, 2012a). These upscaled quantities are influenced by ν_1 and ν_2, which are the parameters representing contributions of sorption nonlinearity and surface diffusion, respectively:

$$\upsilon_1 = \frac{C_{\mu s} - \overline{C}_\mu}{1 + \overline{K}\overline{C}_k} \quad \ldots\ldots\ldots\ldots\ldots\ldots\ldots (19)$$

$$\upsilon_2 = \frac{(1-\overline{\phi}_k)\overline{D}_s \frac{d\overline{K}}{d\overline{\phi}_k}}{\overline{\phi}_k \lambda^2 \overline{C}_{\mu 0}}. \quad \ldots\ldots\ldots\ldots\ldots\ldots (20)$$

Γ_{ex} is a new upscaled quantity that appears because of mass-transfer coupling between the organic and inorganic media. It is defined as

$$\Gamma_{ex} = \frac{\phi_I \sigma^2_{\phi_k}}{2\overline{\phi}_k} \ell_m \left(\frac{\mathrm{d}\overline{D}}{\mathrm{d}\overline{\phi}_k} - \frac{\overline{C}_\mu}{\overline{C} - \overline{C}_k}\frac{\mathrm{d}\overline{D}_s}{\mathrm{d}\overline{\phi}_k}\right)(\overline{C} - \overline{C}_k) [1 - \sqrt{\pi}\,\eta\, e^{\eta^2} \operatorname{erfc}(\eta)], \quad \ldots\ldots\ldots\ldots\ldots (21)$$

where η is a new spatial variable related to the correlation length of the kerogen porosity:

$$\eta = \sqrt{\frac{\ell_m \overline{D}\lambda^2}{4\beta g_m}} = \sqrt{\frac{\ell_m \lambda^2}{4N_{\text{Pe}}}}. \quad \ldots\ldots\ldots\ldots\ldots\ldots (22)$$

In **Fig. 11,** we present the effect of local kerogen heterogeneities on gas permeation during the pressure-pulse-decay experiment discussed earlier. On the left, we show that increasing variability in kerogen porosity leads to retardation in the pressure-pulse decay. On the right, we show that the surface transport (or the so-called hopping) has the potential to decay the pulse and allow the fluid/rock system to reach a new thermodynamic equilibrium state at significantly faster rates. These results are important because they point to a dynamic interplay between the processes that take place in the organic and inorganic porous materials that make up the matrix of organic-rich shale. Clearly, kerogen can affect gas storage and transport. Furthermore, the results indicate that small-scale local phenomena of adsorption and diffusion could lead to significant changes in the global behavior of shale gas transport.

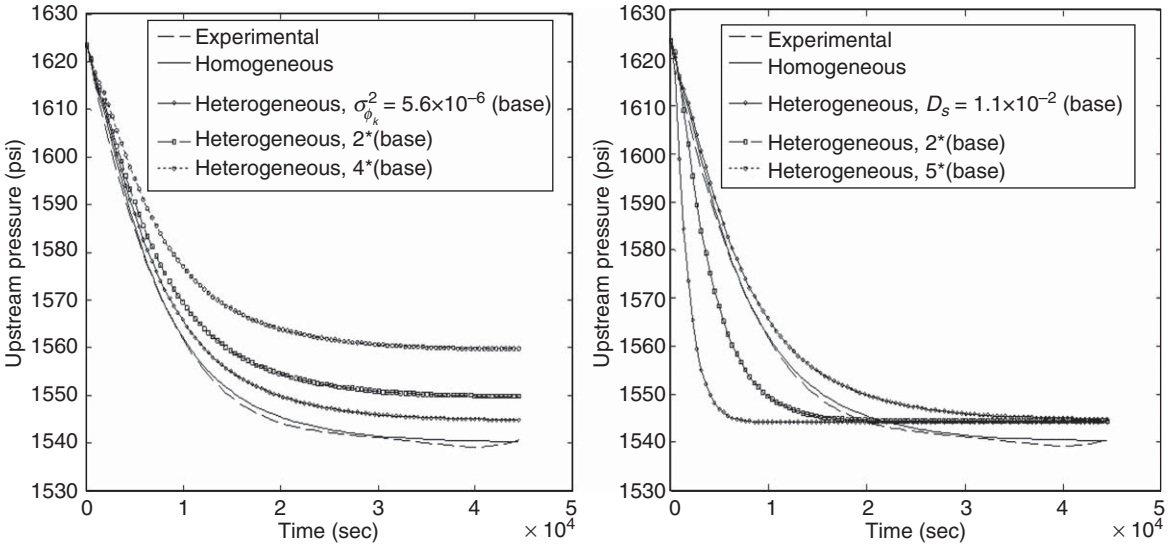

Fig. 11—(a) Effect of kerogen-porosity variance on the pressure-pulse-decay curve. (b) Effect of molecular streaming on the pressure pulse decay curve.

Conclusions

In this paper, a new mathematical formulation is introduced in detail to investigate multiscale gas-transport phenomena in organic-rich-shale core plugs. The formulation is consistent with the microscale observations based on scanning electron microscopy and adsorption porosimetry. It is also inspired by the recent mesoscale LBM simulations. Kerogen is considered a nanoporous organic material finely dispersed within the inorganic matrix. The formulation is used to model and history match gas-permeation measurements in the laboratory using shale core plugs. The results indicate significance of molecular phenomena on gas transport. Adsorbed-phase (surface) transport by the organic pore walls could develop and dominate the gas transport in kerogen as a result of strong gas/solid interactions. In the second part of the paper, we present a novel multiscale perturbation approach to quantify the overall impact of local porosity fluctuations associated with a spatially nonuniform kerogen distribution on the adsorption and transport in shale gas reservoirs. The new upscaled formulation is compared with the previous homogeneous case numerically using finite-difference approximations to initial/boundary value problems simulating the pressure-pulse decay. We show that the presence of kerogen and its impact on porosity heterogeneity are nontrivial and that the transport is sensitive to the molecular phenomena.

The work emphasizes the role kerogen plays in gas storage and transport in shales and could be an important milestone in the development of a new generation of shale-gas-reservoir flow simulators.

Nomenclature

c_p = pore compressibility
C_f = fracture gas concentration
C_k = free-gas concentration in kerogen
C_D = experimental-data covariance matrix
C_M = model-variables covariance matrix
C_μ = adsorbed-gas concentration in kerogen
d_{ui} = unconditional realizations of data
D = tortuosity-corrected coefficient of molecular diffusion
D_k = kerogentortuosity-corrected coefficient of molecular diffusion
$D_{k_{\text{eff}}}$ = effective coefficient of molecular diffusion
D_s = surface diffusion coefficient
g = theoretical model describing the relation between model variables and the observation data
g_m = free gas amount averaged over a large space domain and time interval
k_{ads} = adsorption-kinetics rate coefficient
k_{desorp} = desorption-kinetics rate coefficient
k_f = fracture permeability
k_m = absolute permeability of the inorganic matrix
K = equilibrium partition (or distribution) coefficient
K_L = fracture dispersion coefficient
Kn = Knudsen number
m = vector of model variables
m_{ui} = unconditional realizations of model variables
n = number of iteration
N_{Pe} = dimensionless Péclet number
N_{Th} = Thiele modulus
O = objective function
P = pressure
P_L = Langmuir pressure
R = universal gas constant
t = time
T = absolute temperature
V = velocity
$V_{a\max}$ = Langmuir volume
V_b = matrix bulk volume
V_{center} = velocity at the center
V_{kp} = the kerogen pore volumes
V_{ks} = the kerogen grain volumes
V_p = matrix pore volume
V_{p0} = PV at zero pressure
V_{ms} = matrix grain volume
W_{km} = mass exchange between two continua kerogen and matrix
W_{mf} = mass exchange between two continua matrix and fracture
x = space coordinate
z = gas compressibility
α = effective drift velocity
β = gas mobility
Φ_k = solid-to-bulk kerogen volume ratio
ϕ = total interconnected matrix porosity
ϕ_f = fracture porosity in shale
ϕ_k = kerogen porosity
ε_{kp} = kerogen pore volume per total matrix pore volume
ε_{ks} = total organic content in terms of organic grain volume per total grain volume
μ = dynamic gas viscosity
ρ = density
ρ_{smax} = maximum density of the adsorbed-phase
$\sigma^2_{\phi k}$ = variance of kerogen porosity
λ = kerogen porosity correlation length

ℓ = shape factor
Ψ = diffusive transport
Γ_{tr} = macrotransport effect
Γ_{kn} = macrokinetics effect

Subscripts

f = related to fracture
k = related to kerogen
m = related to matrix

Acknowledgments

The authors thank Devon Energy for financial support provided for this work.

References

Adesida, A., Akkutlu, I.Y., Resasco, D.E. et al. 2011. Kerogen Pore Size Distribution of Barnett Shale Using DFT Analysis and Monte Carlo Simulations. Paper SPE 147397 presented during the SPE Annual Tech. Conf. Exhibition held in Denver, Colorado, 30 October–2 November. http://dx.doi.org/10.2118/147397-MS.

Ambrose, R.J., Hartman, R.C., Diaz-Campos, M. et al. 2012. Shale Gas in-Place Calculations Part I – New Pore-Scale Considerations. *SPE J.* **17** (1): 219–229. http://dx.doi.org/10.2118/131772-PA.

Bear, J. and Bachmat, Y. 1991. *Introduction to Modeling of Transport Phenomena in Porous Media*. New York: Springer.

Brace, W. F., Walsh, J.B., and Frangos, W.T. 1968. Permeability of Granite Under High Pressure. *J. Geophys. Res.* **73** (6): 2225–2236. http://dx.doi.org/10.1029/JB073i006p02225.

Bustin, R.M., Bustin, A.M.M., Cui, X., et al. 2008. Impact of Shale Properties on Pore Structure and Storage Characteristics. Paper SPE 119892 presented during the SPE Shale Gas Production Conference, Fort Worth, Texas, 16–18 November. http://dx.doi.org/10.2118/119892-MS.

Cui, X., Bustin, M.M., and Bustin, R.M. 2009. Measurements of Gas Permeability and Diffusivity of Tight Reservoir Rocks: Different Approaches and their Applications. *Geofluids* **9** (3): 208–223. http://dx.doi.org/10.1111/j.1468-8123.2009.00244.x.

Cushman J. H., Bennethum, L. S., and Hu, X. B. 2002. A Primer on Upscaling Tools for Porous Media. *Adv. Water Resour.* **25** (8–12): 1043–1067. http://dx.doi.org/10.1016/S0309-1708(02)00047-7.

Dietrich, P., Helmig, R., Sauter, M. et al. 2005. *Flow and Transport in Fractured Porous Media*. New York: Springer.

Fathi, E. and Akkutlu, I.Y. 2009. Matrix Heterogeneity Effects on Gas Transport and Adsorption in Coalbed and Shale Gas Reservoirs. *Transp. Porous Media* **80:** 281–304. http://dx.doi.org/10.1007/s11242-009-9359-4.

Fathi E. and Akkutlu, I.Y. 2011. Lattice Boltzmann Method for Simulation of Shale Gas Transport in Kerogen. Paper SPE-146821 presented during the SPE Annual Technical Conference and Exhibition held in Denver, Colorado, 30 October–2 November. http://dx.doi.org/10.2118/146821-MS.

Fathi, E. and Akkutlu, I.Y. 2012a. Mass Transport of Adsorbed-Phase in Stochastic Porous Medium with Fluctuating Porosity Field and Nonlinear Gas Adsorption Kinetics. *Transp. Porous Media* **91** (1): 5–33. http://dx.doi.org/10.1007/s11242-011-9830-x.

Fathi, E. and Akkutlu, I.Y. 2012b. Shale Gas Correction to Klinkenberg Slip Theory. Paper SPE 154977 presented at the Americas Unconventional Resources Conference held in Pittsburgh, Pennsylvania, 5–7 June. http://dx.doi.org/10.2118/154977-MS.

Finsterle, S. and Persoff, P. 1997. Determining Permeability of Tight Rock Samples Using Inverse Modeling. *Water Resour. Res.* **33** (8): 1803–1811. http://dx.doi.org/10.1029/97WR01200.

Forster, D. 1975. *Hydrodynamics Fluctuations Broken Symmetry and Correlation Functions*. Reading, Massachusetts: Benjamin-Cummings.

Freeman, C.M., Moridis, J.M., and Blasingame, T.A. 2011. A Numerical Study of Microscale Flow Behavior in Tight Gas and Shale Gas Reservoir Systems. *Transp. Porous Media* **90:** 253–268. http://dx.doi.org/10.1007/s11242-011-9761-6.

Gelhar, L.W. 1993. *Stochastic Subsurface Hydrology*. Englewood Cliffs, New Jersey: Prentice Hall.

Javadpour, F. 2009. Nanopores and Apparent Permeability of Gas Flow in Mudrocks (Shales and Siltstone). *J. Cdn. Pet. Tech.* **48** (8): 16–21. http://dx.doi.org/10.2118/09-08-16-DA.

Kang, S.M., Fathi, E., Ambrose, R.J. et al. 2011. CO2 Applications. Carbon Dioxide Storage Capacity of Organic-Rich Shales. *SPE J.* **16** (4): 842–855. http://dx.doi.org/10.2118/134583-PA

King, M.R. 2007. Oscillatory Gas Flow in a Circular Nanotube. *The Open Nanoscience Journal* **1** (1): 1–4. http://dx.doi.org/10.2174/1874140100701010001.

L'Heureux, I. 2004. Stochastic Reaction-Diffusion Phenomena in Porous Media with Nonlinear Kinetics: Effects of Quenched Porosity Fluctuations. *Phys. Rev. Lett.* **93** (18): 180602. http://dx.doi.org/10.1103/PhysRevLett.93.180602.

Ning, X. 1992. The Measurement of Matrix and Fracture Properties in Naturally Fractured Low Permeability Cores Using a Pressure Pulse Method. PhD dissertation, Texas A&M University, College Station, Texas.

Oliver, D.S., Reynolds, A.C., and Liu, N. 2008. *Inverse Theory for Petroleum Reservoir Characterization and History Matching*. New York: Cambridge University Press.

Oliver, D.S., He, N., and Reynolds A.C. 1996. Conditioning Permeability Fields to Pressure Data. Proc. European Conference for the Mathematics of Oil Recovery, Leoben, Austria, 3–6 September.

Schlebaum, W., Schraa, G., and Van Riemsdijk, W.H. 1999. Influence of Nonlinear Sorption Kinetics on the Slow Desorbing Organic Contaminant Fraction in Soil. *Environ. Sci. Technol.* **33:** 1413–1417. http://dx.doi.org/10.1021/es980233e.

Schettler, P.D. and Parmely, C.R. 1991. Contributions to Total Storage Capacity in Devonian Shales. Paper SPE 23422 presented at the SPE Eastern Regional Meeting, Lexington, Kentucky, 22–25 October. http://dx.doi.org/10.2118/23422-MS.

Sondergeld, C.H., Ambrose, R.J., Rai, C.S., et al. 2010a. Micro-Structural Studies of Gas Shales. Paper SPE 131771 presented during the SPE Unconventional Gas Conference held in Pittsburgh, Pennsylvania, 23–25 February. http://dx.doi.org/10.2118/131771-MS.

Sondergeld, C.H., Newsham K.E., Comisky J.T., et al. 2010b. Petrophysical Considerations in Evaluating and Producing Shale Gas Resources. Paper SPE-131768 presented during the SPE Unconventional Gas Conference held in Pittsburgh, Pennsylvania, 23–25 February. http://dx.doi.org/10.2118/131768-MS.

Srinivasan, R., Auvil, S.R., and Schork, J.M. 1995. Mass Transfer in Carbon Molecular Sieves—An Interpretation of Langmuir Kinetics. *Chem. Eng. J.* **57:** 137–144. http://dx.doi.org/10.1016/0923-0467(94)02942-3.

Succi, S. 2001. *The lattice Boltzmann equation for fluid dynamics and beyond*. Oxford University Press, Oxford.

Wang, F.P. and Reed, R.M. 2009. Pore Networks and Fluid Flow in Gas Shales. Paper SPE 124253 presented during the Annual Technical Conference and Exhibition held in New Orleans, Louisiana, 4–7 October. http://dx.doi.org/10.2118/124253-MS.

I. Yucel Akkutlu is an associate professor of petroleum engineering at the Texas A&M University. His current academic research is in thermodynamics of fluids in nanoporous materials, and in scaling up and homogenization of coupled transport and reaction processes in low-permeability geological formations exhibiting multiscale pore structures. Akkutlu holds MSc and PhD degrees in petroleum engineering from the University of Southern California. Akkutlu currently serves on the Natural Sciences and Engineering Research Council of Canada as a member of the Materials and Chemical Engineering Committee. He is the Executive Editor of the *SPE Journal.*

Ebrahim Fathi is assistant professor of petroleum engineering at West Virginia University. Fathi earned BS and MSc degrees from Tehran University and a PhD degree in petroleum engineering from the University of Oklahoma. His research interests are unconventional reservoir engineering and natural-gas production, multiscale reservoir simulation, and upscaling of the fluid flow, transport, and reaction processes in heterogeneous porous media.